CrossMark

J. Plasma Phys. (2023), *vol*. 89, 905890208 © The Author(s), 2023.
Published by Cambridge University Press
This is an Open Access article, distributed under the terms of the Creative Commons Attribution licence (http://creativecommons.org/licenses/by/4.0), which permits unrestricted re-use, distribution and reproduction, provided the original article is properly cited.
doi:10.1017/S0022377823000120

Particle-in-cell simulations of Alfvén wave parametric decay in a low-beta plasma

C.A. González [1],†, **Maria Elena Innocenti** [2] **and Anna Tenerani** [1]

[1]Department of Physics, The University of Texas at Austin, Austin, TX 78712, USA

[2]Institut für Theoretische Physik, Ruhr-Universität Bochum, Bochum, Germany

(Received 14 December 2022; revised 23 January 2023; accepted 24 January 2023)

We study the parametric decay instability of parallel-propagating Alfvén waves in a low-beta plasma using one-dimensional fully kinetic simulations. We focus for the first time on the conversion of the energy stored in the initial Alfvén wave into particle internal energy, and on its partition between particle species. We show that compressible fluctuations generated by the decay of the pump wave into a secondary ion-acoustic mode and a reflected Alfvén wave contribute to the gain of internal energy via two distinct mechanisms. First, the ion-acoustic mode leads nonlinearly to proton trapping and proton phase-space mixing, in agreement with previous work based on hybrid simulations. Second, during the nonlinear stage, a compressible front of the fast type develops at the steepened edge of the backward Alfvén wave leading to a field-aligned proton beam propagating backwards at the Alfvén speed. We find that parametric decay heats preferentially protons, which gain approximately 50 % of the pump wave energy in the form of internal energy. However, we find that electrons are also energized and that they contribute to the total energy balance by gaining 10 % of the pump wave energy. By investigating energy partition and particle heating during parametric decay, our results contribute to the determination of the role of compressible and kinetic effects in wave-driven models of the solar wind.

Key words: plasma waves, plasma heating, plasma instabilities

1. Introduction

Alfvén waves are ubiquitous in magnetized plasmas and represent one of the building blocks of many phenomena in space and in the laboratory. Alfvén waves are also thought to play a crucial role in coronal heating and solar wind acceleration. By propagating almost undisturbed along the magnetic field, they provide a means to transport energy from the photosphere to the corona and further out (Del Zanna & Velli 2002). Alfvén-wave-like correlation of magnetic and velocity field fluctuations is commonly observed in the solar wind (Coleman 1967; Belcher & Davis 1971), providing support to wave-driven wind theories (see e.g. Cranmer 2012). Understanding how the energy carried by Alfvén waves is ultimately converted and released to the plasma in the form of internal energy is therefore key to our understanding of coronal heating and solar wind acceleration.

† Email address for correspondence: carlos.gonzalez1@austin.utexas.edu

https://doi.org/10.1017/S0022377823000120 Published online by Cambridge University Press

Large-amplitude Alfvén waves at magnetohydrodynamic scales are unstable to parametric decay instability (PDI). In a low-beta plasma (when the thermal pressure is smaller than the magnetic pressure), PDI leads to the decay of the 'pump' wave into a forward ion-acoustic wave and a lower-frequency backward Alfvén wave (Galeev & Oraevskii 1973; Derby 1978). The PDI is of great interest, first, because it provides a mechanism to generate reflected Alfvén waves which are essential to trigger the turbulent cascade (Chandran 2018; Malara, Primavera & Veltri 2022) – the latter providing a possible mechanism to heat and accelerate the plasma (e.g. Perez & Chandran 2013). Second, the PDI generates also compressible modes that in turn contribute to heat the plasma via formation of shocks (Del Zanna, Velli & Londrillo 2001) or, when proton kinetic effects are retained, via particle trapping and phase-space mixing (Araneda *et al.* 2008; Matteini *et al.* 2010*b*), and proton energization at steepened fronts (González *et al.* 2020, 2021). Since the growth rate increases with decreasing plasma beta, theory and simulations predict that this instability should contribute to the dynamics of the solar wind in the inner heliosphere, preferentially in regions close to the sun where $\beta \ll 1$ (Tenerani & Velli 2013; Réville, Tenerani & Velli 2018). Recently, signatures consistent with PDI in the lower solar atmosphere have been reported (Hahn, Fu & Savin 2022), providing support to scenarios that invoke parametric decay, and in general the generation of compressible modes, to drive fast wind streams (Suzuki & Inutsuka 2005; Shoda *et al.* 2019; Verdini, Grappin & Montagud-Camps 2019).

Despite the vast body of work investigating parametric instabilities of parallel-propagating (e.g. Sakai & Sonnerup 1983; Wong & Goldstein 1986; Jayanti & Hollweg 1993; Nariyuki & Hada 2007) and oblique-propagating (Vasquez & Hollweg 1996; Del Zanna 2001; Matteini *et al.* 2010*a*; Del Zanna *et al.* 2015) Alfvén waves, the heating processes resulting from the coupling between Alfvén and compressible modes remain poorly understood from a kinetic perspective. Among the most prominent issues still not fully investigated is how much of the energy carried by the pump wave goes into internal energy, and how the latter is partitioned between protons and electrons. This is fundamental for understanding the role of PDI in solar wind heating and acceleration. Indeed, *in situ* and remote-sensing observations have found preferential heating of ions relative to electrons (Wilson *et al.* 2018; Cranmer 2020) and in general there is a well-known positive correlation between solar wind speed and proton temperature (Elliott *et al.* 2012), whereas the solar wind speed is anti-correlated with the coronal electron temperature (Geiss *et al.* 1995). If PDI contributes significantly to coronal plasma heating, it must be consistent with those constraints.

The goal of this work is to investigate electron kinetic effects during the parametric decay of a parallel-propagating Alfvén wave and to determine how the initial energy stored in the pump wave is partitioned between the internal energy of protons and electrons. So far, only a few works have studied parametric instabilities with a fully kinetic particle-in-cell (PIC) approach (Sakai *et al.* 2005; Nariyuki, Matsukiyo & Hada 2008). Those works have considered reduced mass ratio ($m_i/m_e = 16$) and a smaller wavelength for the pump wave. However, in order to understand if large-scale processes can affect the electron population, one has to maintain a large scale separation between electrons and ions. A lower mass ratio would increase the relative electron gyroradius, possibly introducing artificial electron heating, e.g. via unrealistic particle scattering at magnetic structures. Here we perform PIC simulations of a weakly dispersive circularly polarized Alfvén wave with a more realistic electron-to-proton mass ratio in one dimension; $m_i/m_e = 400$ ensures that electron and ion scales are well separated while at the same time significantly reducing the computational cost of resolving the electron scales (needed for the explicit PIC simulation) with respect to a realistic mass ratio simulation with the

https://doi.org/10.1017/S0022377823000120 Published online by Cambridge University Press

same size in terms of ion skin depths. We compare results from hybrid and PIC models, and consider different proton-to-electron temperature ratio and total plasma beta. For the PIC simulations we use the semi-implicit, energy-conserving ECsim code (Lapenta 2017; Lapenta, Gonzalez-Herrero & Boella 2017; Gonzalez-Herrero, Boella & Lapenta 2018) and the explicit VPIC code (Bowers *et al.* 2008*b*, *a*, 2009). The semi-implicit algorithm allows us to resolve only the scales of interest without resolving the Debye length as in explicit PIC codes. This feature will be useful in future work in two and three dimensions when explicit simulations become prohibitively expensive. In addition, we run hybrid simulations with the CAMELIA code (Matthews 1994; Franci *et al.* 2018) as a reference for the decay process and proton heating in the absence of electron kinetic effects.

In § 2 we describe the model and simulation set-up and in § 3 we present the main results. The conclusions of this study are summarized in § 4.

2. Model and simulation set-up

We consider a large-amplitude, monochromatic Alfvén wave propagating parallel to the mean magnetic field $\boldsymbol{B}_0$, taken along the x axis. The initial perturbation for the electromagnetic field is given by $\delta B_y = \delta B \sin(k_0 x)$, $\delta B_z = -\delta B \cos(k_0 x)$, $E_y = -\delta B\, \omega_0/(k_0 c) \cos(k_0 x)$ and $E_z = -\delta B\, \omega_0/(k_0 c) \sin(k_0 x)$. The current density is carried by both species, and is initialized in order to satisfy Ampere's law with an initial drifting Maxwellian distribution with mean proton and electron velocities given by (Sakai *et al.* 2005)

$$\delta \boldsymbol{u}_i = \left(\frac{(\omega_0 + \Omega_{ce})(\omega_0^2 - c^2 k_0^2)}{(\omega_{pe}^2 + \omega_{pi}^2) k_0} - \frac{\omega_0}{k_0} \right) \frac{\delta \boldsymbol{B}}{B_0}, \tag{2.1a}$$

$$\delta \boldsymbol{u}_e = \left(\frac{(\omega_0 - \Omega_{ci})(\omega_0^2 - c^2 k_0^2)}{(\omega_{pe}^2 + \omega_{pi}^2) k_0} - \frac{\omega_0}{k_0} \right) \frac{\delta \boldsymbol{B}}{B_0}, \tag{2.1b}$$

where $\omega_{p\alpha} = \sqrt{e^2 n_\alpha / \epsilon_0 m_\alpha}$ and $\Omega_{c\alpha} = q_\alpha \boldsymbol{B}/m_\alpha$ are the plasma frequency and the gyrofrequency of species $\alpha = i, e$. The initial wave frequency ω_0 is obtained from the dispersion relation of parallel-propagating waves in a two-fluid plasma (Baumjohann & Treumann 2012):

$$\frac{k^2 c^2}{\omega^2} = 1 - \frac{\omega_{pe}^2}{\omega(\omega + \Omega_{ce})} - \frac{\omega_{pi}^2}{\omega(\omega - \Omega_{ci})}. \tag{2.2}$$

In the rest of the paper we present our results using the following normalization. The magnetic field and density fluctuations are expressed in units of the guide-field magnitude B_0 and of the initial plasma density $n_0 = n_{i_0} = n_{e_0}$, respectively. Lengths are normalized to the proton inertial length $d_i = c/\omega_{p_i}$, time is expressed in units of the inverse of proton gyrofrequency Ω_{ci}^{-1} and the velocities are normalized to the proton Alfvén speed $v_A = B_0/\sqrt{4\pi n_0 m_i}$. The plasma beta for both protons and electrons is defined as $\beta_{i,e} = 2 n_0 k_B T_{i,e}/B_0^2$. The electron characteristic scales are related to the proton scales through the mass ratio that we fixed to $m_i/m_e = 400$ for the PIC simulations. We considered an initial weakly dispersive pump wave with a wavenumber $m_0 = 4$ and wave vector $k_0 = 2\pi m_0/L$, L being the size of the simulation domain. The initial wave amplitude is $\delta B/B_0 = 0.5$ and the wave propagates with a phase velocity $\omega_0/k_0 = 0.885 v_A$, with $v_A/c = 0.05$ and $k_0 d_i = 0.2454$. A similar set-up for the magnetic and the velocity fields is used to initialize the hybrid simulation (in the limit $\Omega_{ce} \gg \omega$). A summary of the numerical parameters for the simulations presented here can be found in table 1. We

https://doi.org/10.1017/S0022377823000120 Published online by Cambridge University Press

Run	$L_x(d_i)$	$\Delta x(d_i)$	$\Delta t(\Omega_{ci}^{-1})$	ppc	β	β_i	β_e	T_i/T_e
Hyb-TiTe1	102.4	0.1	0.005	10 000	0.25	0.125	0.125	1
Vpic-TiTe1	102.4	0.0125	0.000125	500	0.25	0.125	0.125	1
ECsim-TiTe1	102.4	0.025	0.0005	500	0.25	0.125	0.125	1
ECsim-TiTe1B	102.4	0.025	0.0005	500	0.1575	0.078125	0.078125	1
ECsim-TiTe4	102.4	0.025	0.0005	500	0.1575	0.03248	0.125	4

TABLE 1. Initial conditions for the simulations presented in this paper.

compare the results of simulations with the same plasma beta and different temperature ratio between electrons and protons (ECsim-TiTe1B and ECsim-TiTe4) with simulations with the same temperature ratio and different beta (ECsim-TiTe1 and ECsim-TiTe1B), to separate the effects of the two parameters.

3. Results

3.1. *Overview*

Figures 1 and 2 provide an overview of the time evolution of the parametric decay in the simulations listed in table 1. We show, from top to bottom, the variation of the normalized root mean square (r.m.s.) of the magnetic and total density fluctuations, the correlation between velocity and magnetic field fluctuations ($\rho_{vB} = \boldsymbol{v} \cdot \boldsymbol{B}/\|\boldsymbol{v}\|\|\boldsymbol{B}\|$), the r.m.s. of the field-aligned electric field e_x, and the variation of the mean proton and electron temperatures normalized to their initial value. The growth rate of the PDI is reported in the legend and corresponds to the slope of the best fit indicated by the red solid line in the second panel down of each figure.

In figure 1 we compare results from the hybrid simulation and from the explicit (VPIC) and the semi-implicit (ECsim) PIC simulations, for $T_i = T_e$ and $\beta_e = 0.125$. The decay of the pump wave, marked by the exponential growth of density fluctuations (second panel), proceeds similarly in the hybrid and PIC simulations. In both models the decay starts at the same time, around $t\Omega_{ci} \simeq 150$, with the density fluctuations growing at the same rate. The saturation of the instability occurs when the backward-propagating Alfvén wave and forward-propagating ion-acoustic wave are well developed and density fluctuations reach a constant value of $\delta n_{rms}/\langle n \rangle \simeq 0.2$ at around $t \simeq 225\Omega_{ci}^{-1}$ (vertical dashed line). A complete reflection of the pump wave then takes place, as can be seen from the third panel, when the sign of ρ_{VB} changes from -1 to $+1$. During this stage, a portion of the initial magnetic energy is converted into kinetic and internal energy of both protons and electrons. In particular, protons undergo strong parallel heating along the local magnetic field with significant perpendicular heating (fifth and bottom panels), as reported in previous studies (González *et al.* 2020). The PIC simulations show that electrons are not isothermal during the decay process and that they are also energized. The heating of electrons is on average isotropic and proceeds at nearly a constant rate. This can be seen from the bottom panels of figure 1, showing that $T_{e\parallel} \simeq T_{e\perp}$ and that temperatures keep increasing during the nonlinear stage (specifically after $t\Omega_{ci} \simeq 500$). We noticed a small difference in the electron temperature for the explicit and semi-implicit simulations with a slightly larger final temperature in the VPIC simulation. This might be due to numerical heating associated with explicit codes, although the relative error of the total energy is less than 1 % in both simulations.

https://doi.org/10.1017/S0022377823000120 Published online by Cambridge University Press

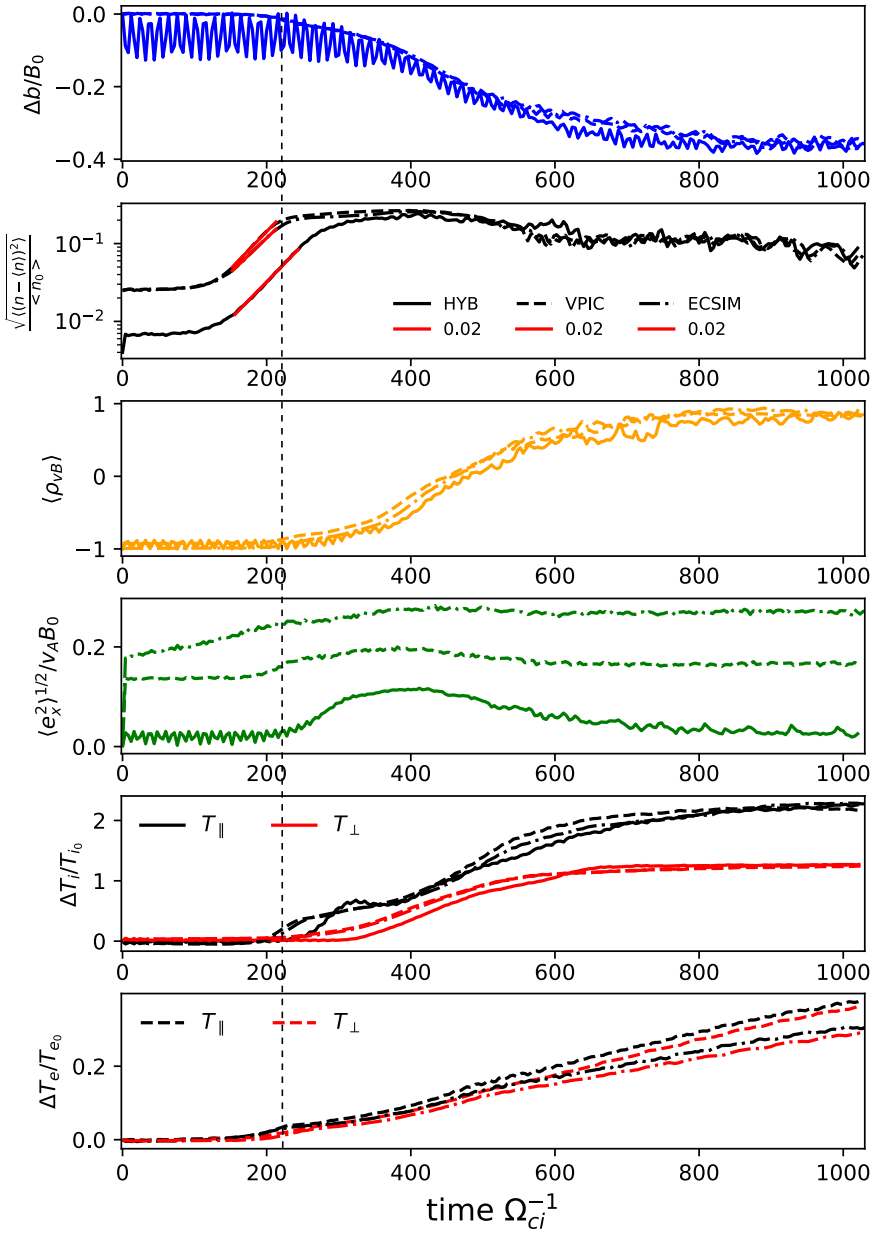

FIGURE 1. Temporal evolution of the variation of the r.m.s. of magnetic field fluctuations (top panel), r.m.s. of total density fluctuations (second panel), the correlation between magnetic and velocity fluctuations ρ_{VB} (third panel) and r.m.s. of the field-aligned electric field (fourth panel). The fifth and bottom panels show the variation of the proton and electron mean parallel and perpendicular temperatures.The vertical black dashed lines represent the end of the linear stage of PDI for Ecsim-TiTe1.

https://doi.org/10.1017/S0022377823000120 Published online by Cambridge University Press

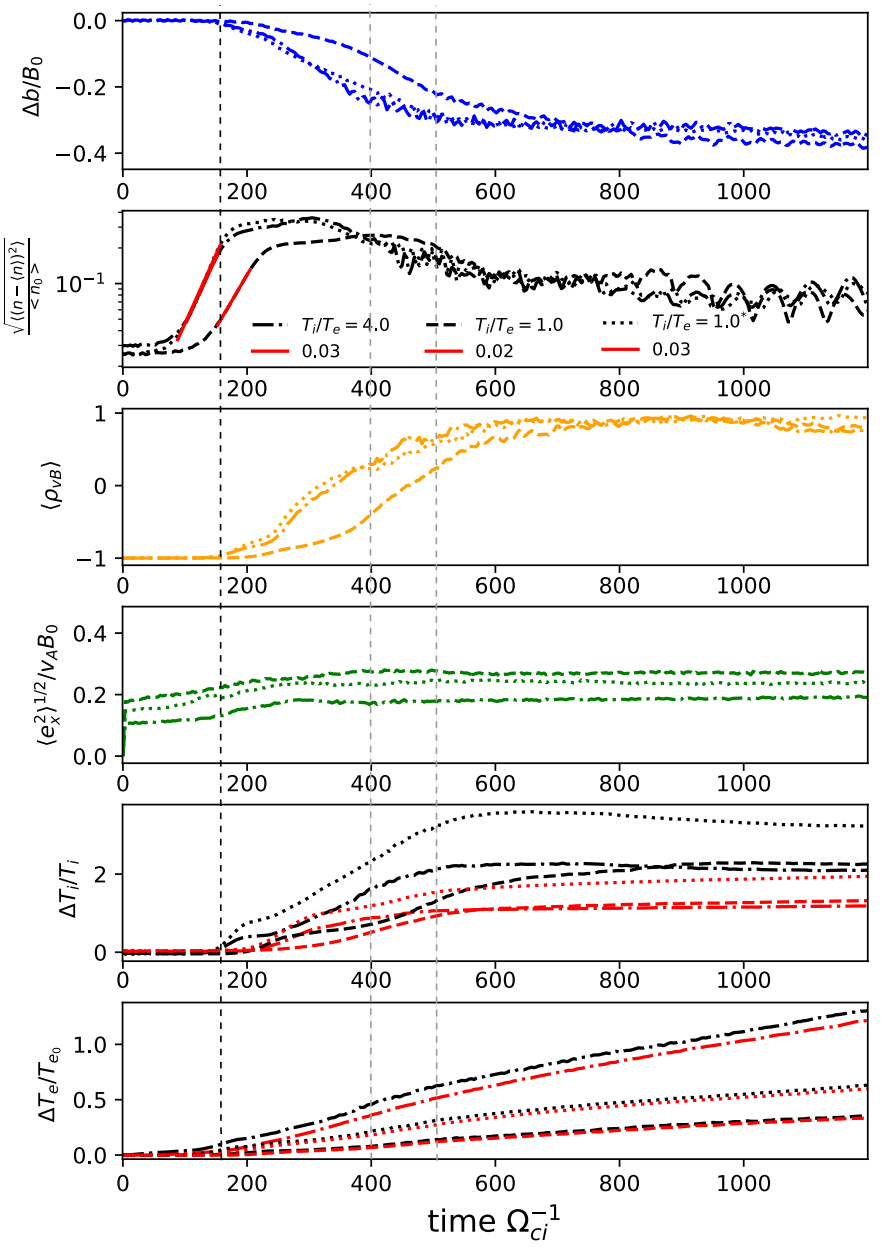

FIGURE 2. Temporal evolution of the variation of the r.m.s. of magnetic field fluctuations (top panel), r.m.s. of total density fluctuations (second panel), the correlation between magnetic and velocity fluctuations ρ_{VB} (third panel) and r.m.s. of the field-aligned electric field (fourth panel). The fifth and bottom panels show the variation of the proton and electron mean parallel and perpendicular temperatures. Results for runs Ecsim-TiTe4 (dot-dashed line), Ecsim-TiTe1 (dashed line) and Ecsim-TiTe1B (dotted line). The vertical black dashed lines represent the end of the linear stage of PDI for Ecsim-TiTe4 and Ecsim-TiTe1B. The grey dashed lines mark the times when distribution functions are shown in figure 3.

https://doi.org/10.1017/S0022377823000120 Published online by Cambridge University Press

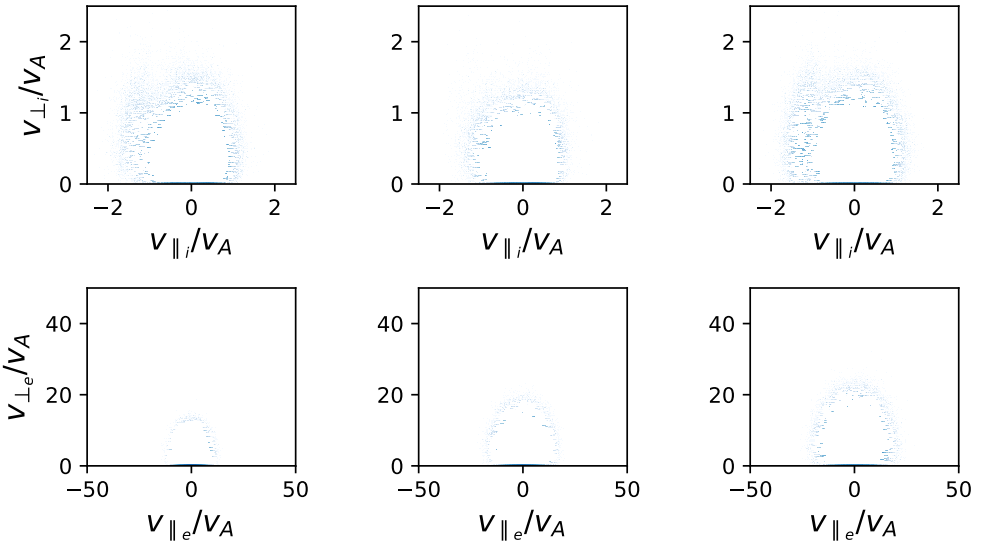

FIGURE 3. Reduced particle VDFs for protons (top) and electrons (bottom) integrated over the entire domain. Shown, from left to right, are the VDFs for Ecsim-TiTe4, Ecsim-TiTe1 and Ecsim-TiTe1B, at $t = 400\Omega_{ci}^{-1}$, $t = 560\Omega_{ci}^{-1}$ and $t = 400\Omega_{ci}^{-1}$, respectively.

Figure 2 shows results for simulations performed with ECsim with different β and proton-to-electron temperature ratio T_i/T_e. As can be seen from these plots, the total plasma β determines the growth rate and the overall decay of the pump wave in agreement with fluid theory (Wong & Goldstein 1986; Hollweg 1994), which predicts that higher-beta plasmas have a lower growth rate. This dependence can be seen by comparing runs ECSim-TiTe4 (dot-dashed) and TiTe1B (dotted), which have different electron temperature but the same total plasma beta, and by comparing ECSim-TiTe1B and TiTe1, corresponding to different values of the plasma beta. We observe that the higher the initial T_e, the higher the electric field, in agreement with the dependence of the electric field on β_e from the generalized Ohm's law.

The most significant difference between the simulations with the same beta but different T_i/T_e is registered in the r.m.s. of the electric field (second column, fourth panel: dotted versus dot-dashed line). We observe lower r.m.s. values of e_x when $T_i > T_e$. This is consistent with Landau damping of the ion-acoustic mode, which is expected to be stronger when $T_i > T_e$ than in the case where $T_i = T_e$. Linear Landau damping, however, is not strong enough to affect the growth of the instability.

To conclude our overview of the decay process, in figure 3 we show the contour plots of the velocity distribution functions (VDFs) in velocity space, $f(v_\parallel, |v_\perp|)$, integrated in x. We plot the VDFs of protons (top panels) and electrons (bottom panels) when the system has achieved the nonlinear stage for runs ECSim-TiTe4, ECSim-TiTe1 and ECSim-TiTe1B. This time is marked by the vertical grey dashed lines in figure 2, at $t = 400\Omega_{ci}^{-1}$, $t = 560\Omega_{ci}^{-1}$ and $t = 400\Omega_{ci}^{-1}$ for each simulation, respectively. As is discussed in the next sections, protons develop an anisotropic distribution function with a clear field-aligned beam propagating backward, and an energized field-aligned population at the (positive) ion-acoustic speed (see figure 6 for more details). Electrons instead remain on average isotropic, and their heating is much less pronounced than proton heating.

https://doi.org/10.1017/S0022377823000120 Published online by Cambridge University Press

3.2. *Energy conversion and particle heating*

The energy lost by the pump wave powers the formation of daughter waves and results in thermal and parallel bulk energy gain for protons and electrons. The PIC simulations show that, after the decay of the pump wave, most of the particle internal energy gain goes into proton internal energy. In figure 4, we analyse the pump wave energy conversion and partition by breaking down the total energy (per unit volume) into its contributions from Alfvén wave energy (top panel), parallel kinetic energy (thus including the contribution from the ion-acoustic wave; second panel) and internal energy of protons and electrons (third and bottom panels). All quantities are expressed as variations from their initial value, and they are normalized to the initial pump wave energy $E_{w0} = E_{B_\perp}(0) + E_{v_\perp}(0)$, where

$$E_{B_\perp}(t) = 1/2\langle B_y(t)^2 + B_z(t)^2\rangle \tag{3.1}$$

is the magnetic energy density and

$$E_{v_\perp}(t) = \sum_\alpha 1/2\langle m_\alpha n_\alpha (u_{y_\alpha}(t)^2 + u_{z_\alpha}(t)^2)\rangle \tag{3.2}$$

is the bulk kinetic energy and the brackets denote spatial average. The x component of the kinetic energy is defined as

$$E_{v_\parallel}(t) = \sum_\alpha 1/2\langle m_\alpha n_\alpha u_{x_\alpha}(t)^2\rangle \tag{3.3}$$

and the internal energy of species α as

$$E_{th,\alpha} = 1/2\langle Tr(P_{ij,\alpha})\rangle. \tag{3.4}$$

Energy balance is quantitatively similar in all our simulations. The top panel of figure 4 shows that the energy contained in the Alfvén waves decreases with $|\Delta E_w|/E_{w0} \simeq 60\,\%$. Notice that this does not correspond to the total pump wave energy decrease. The pump wave fully decays in the simulations considered here (see the correlation ρ_{vb} in figure 2). After the decay ($\rho_{vb} = +1$ after $t\Omega_{ci} \gtrsim 500$), 40 % of the pump wave energy goes into a reflected Alfvén wave, and the remaining 60 % goes in an ion-acoustic mode and other forms of internal energy. The second panel, as well as the trend of ρ_{rms} reported in figure 2, shows that at the end of the linear stage (indicated by the vertical dashed line for the case $T_i/T_e = 4$), $\Delta E_\parallel$ has increased due to the growth of the ion-acoustic mode. The subsequent peak of $E_\parallel$, however, is due to the ongoing particle trapping by the ion-acoustic mode that generates a population of protons moving at approximately the ion-sound speed, as discussed in § 3.3 and, for example, in Matteini *et al.* (2010*b*). Particle trapping and subsequent phase-space mixing ultimately lead to the dissipation of the ion-acoustic mode and particle heating. After the complete decay of the pump wave, most of the Alfvén wave energy has gone into proton internal energy. In particular, we find that approximately 50 % of the initial pump wave energy goes into proton internal energy and 10 % to electron internal energy. Notice that, unlike protons, electrons keep heating at a constant rate when the instability has saturated and the pump wave has decayed. At the end of the simulation, the electron internal energy is a factor of 2 larger than the energy at the end of the complete decay ($t\Omega_{ci} \gtrsim 500$). Still, the good energy conservation in the simulations and similar results between explicit and semi-implicit simulations suggest that the electron heating is indeed physical and not a numerical artefact. Such an energy balance appears to be unaffected by the total plasma beta and only slightly by T_i/T_e and m_i/m_e (not shown).

https://doi.org/10.1017/S0022377823000120 Published online by Cambridge University Press

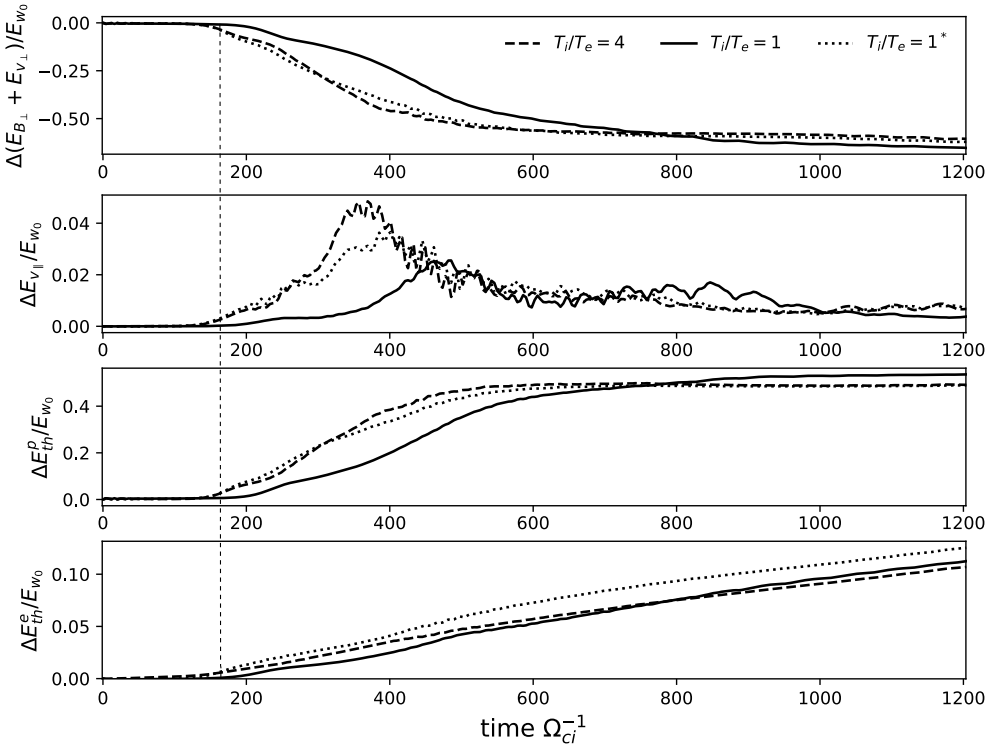

FIGURE 4. Energy conversion and partition. Variation of the wave energy (top panel), of the field-aligned bulk kinetic energy (second panel) and the internal energy variations for protons and electrons (third and bottom panels, respectively). Each panel shows results for runs Ecsim-TiTe4 (dashed), Ecsim-TiTe1 (solid) and Ecsim-TiTe1B (dotted). The vertical dashed line indicates the end of the linear stage for the case $T_i/T_e = 4$.

3.3. *Phase-space dynamics*

Compressibility plays an important role in proton and electron energization and in providing paths to particle heating. In the low-beta simulations presented in this work, we were able to identify and distinguish two types of compressible fluctuations generated during parametric decay: an ion-acoustic mode and a compressible steepened front of the fast-mode type propagating at the Alfvén speed. Such signatures were difficult to discern in higher-beta simulations (González *et al.* 2020). Both types of compressible fluctuations contribute to the increase of internal energy. However, they lead to fundamentally different phase-space dynamics and to different kinetic features. The ion-acoustic mode contributes nonlinearly to phase-space mixing via particle trapping. On the other hand, the development of the steepened front with non-constant $|\boldsymbol{B}|$ leads to the formation of strong parallel heat fluxes and ultimately causes the acceleration of a population of protons into a well-defined beam of particles and the enhancement of proton perpendicular heating. In the following, we analyse the signatures of these processes in the fields and particle VDFs.

In figure 5 (left column) we show contour plots in the (t, x) plane of B_y (figure 5*a*), of the magnetic field magnitude $|\boldsymbol{B}|$ (figure 5*b*) and of the electric field e_x (figure 5*c*). We also plot the scalar pressure agyrotropy (Aunai, Hesse & Kuznetsova 2013;

https://doi.org/10.1017/S0022377823000120 Published online by Cambridge University Press

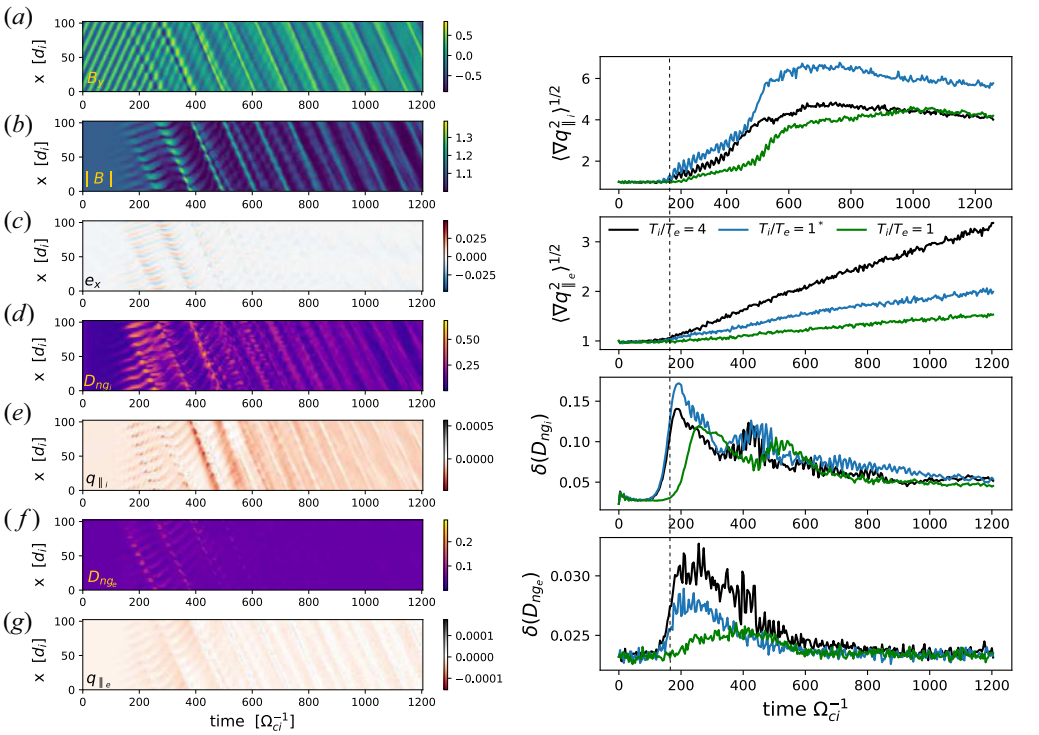

FIGURE 5. Left panels: contour plot in the (t, x) plane of the b_y component (a), the magnitude of the magnetic field (b), the field-aligned component of electric field (c), and the scalar agyrotropy (d) and heat flux (e) for protons and the scalar agyrotropy (f) and heat flux (g) for electrons. Results are shown for ECSim-TiTe4. Right panels: r.m.s. of the divergence of the parallel heat flux for protons (top panel) and electrons (second panel), and variance of the agyrotropy for protons (third panel) and electrons (bottom panel) for all simulations.

Cazzola *et al.* 2016),

$$D_{ng} = \sqrt{8\left(P_{xy}^2 + P_{xz}^2 + P_{yz}^2\right)}/(P_{\parallel}+2P_{\perp}), \tag{3.5}$$

and the parallel heat flux ($q_{\parallel}$) for protons (figure 5*d*,*e*) and electrons (figure 5*f*,*g*), respectively. The thermal energy flux is obtained by calculating the total energy flux for each species ($\boldsymbol{Q}_s = \frac{1}{2} m_s \int f_s(\boldsymbol{x}, \boldsymbol{v}, t) v^2 \boldsymbol{v}\, \mathrm{d}^3\boldsymbol{v}$) and subtracting the energy flux components in the Eulerian frame ($\boldsymbol{q}_s = \boldsymbol{Q}_s - \boldsymbol{H}_s - \boldsymbol{K}_s$), namely the contribution from the bulk energy flux ($\boldsymbol{K}_s = \boldsymbol{u}_s(\rho u_s^2/2)$) and the enthalpy flux ($\boldsymbol{H}_s = P_s \cdot \boldsymbol{u}_s + \boldsymbol{u}_s U_{th}$). This requires the calculation of the lower moments of the velocity distribution (see details in Lapenta *et al.* (2020)). We show results from ECSim-TiTe4 as a reference, since ECSim-TiTe1 and ECSim-TiTe1B are similar. In the right column of figure 5 we show the r.m.s. of the divergence of the parallel heat flux (normalized to its initial value) and the standard deviation of the scalar agyrotropy for both species and for all simulations.

From figure 5 (left column) one can see that a dominant backward-propagating mode forms at $t\Omega_{ci} \simeq 200$, when the PDI has reached saturation. The signature of the forwards ion-acoustic mode can be seen in the plots of e_x in the time interval $t\Omega_{ci} = 200$–400, before it dissipates, corresponding to a wave vector $k_s = 7 \times 2\pi/L_x$. At about $t\Omega_{ci} \simeq 400$, a steepened front propagating backwards at the Alfvén speed also develops. This

https://doi.org/10.1017/S0022377823000120 Published online by Cambridge University Press

steepened front corresponds to a localized increase of $|\boldsymbol{B}|$, positively correlated with a density enhancement. As discussed in our previous work (González *et al.* 2020, 2021), compressive fluctuations in $|\boldsymbol{B}|$ are associated with a field-aligned electric field e_x. Enhancements of e_x at the steepened front can also be seen in figure 5(*c*). The strongest non-thermal features (agyrotropy and heat fluxes) of particles develop at such a steepened front and within the ion-acoustic mode, as shown in figure 5(*c–g*).

The cumulative contribution of non-Larmor particle motion produces non-zero values of the off-diagonal terms of the pressure tensor, quantified by D_{ng}, where local values of up to $|D_{ng,e}| \simeq 0.3$ and $|D_{ng,i}| \simeq 0.65$ are reached. The variance of D_{ng} for both species is reported in the third and fourth panels on the right-hand side of figure 5, and the r.m.s. of the divergence of the parallel heat flux in the first two panels. Agyrotropy in particular is considered one of the VDF-based dissipation measures (Pezzi *et al.* 2021). From figure 5 (right panels) one can see that agyrotropy first builds up during the linear stage of the PDI for both species in correspondence with the ion-acoustic mode, before decaying during the nonlinear stage as the ion-acoustic mode is dissipated and, correspondingly, the plasma is heated. However, protons, unlike electrons, undergo a two-step heating process. Besides particle trapping, protons subsequently interact with the steepened front, where they develop a second peak of agyrotropy. Interaction of protons with a field-aligned discontinuity and electric field causes both proton scattering in phase space, contributing to heating, and the acceleration of protons into a field-aligned beam (González *et al.* 2021). This is consistent with the observed time evolution of proton agyrotropy and parallel heat flux (see top and third panels on the right-hand side of figure 5). Electrons, which have a smaller gyroradius than protons, display on average $D_{ng,e} \ll D_{ng,i}$ (bottom right panel) and, accordingly, they do not gain much internal energy.

Kinetic features in phase space corresponding to the dynamical evolution described above can be seen in figure 6, where we show the proton and electron VDFs in the $(x, v_\parallel)$ space (top) and $(x, v_\perp)$ space (bottom) at $t\Omega_{ci} = 400$. We show results for EcsimTiTe4 only since similar features develop in the other simulations. Protons in phase space are shown on the left and electrons on the right. For reference, we plot $B_y(x)$ (green colour) and $|\boldsymbol{B}(x)|$ (red colour) at the same time to show that the particle beam forms at the steepened front. The contour plot of $f(x, v_\parallel)$ shows the two sources of the proton internal energy increase discussed above. First, saturation of the growth of the ion-acoustic mode is determined by nonlinear particle trapping. The latter causes the formation of a second proton population that propagates forwards at the ion-acoustic speed, and develops well-known signatures of phase-space mixing (vortexes). Second, a proton beam is generated locally at the backward-propagating steepened Alfvén front. The latter can be identified in figure 6 at around $x \simeq 85\, d_i$, and has a size of a few d_i. Both particle trapping and beam formation cause the large increase of the parallel proton temperature and parallel heat flux. One can see in the bottom left-hand panel that also perpendicular heating takes place at the steepened edge, where particles with high perpendicular velocities are observed. The perpendicular energization is due to particle scattering at those discontinuities (González *et al.* 2021). The electrons are also characterized by a local deviation from Maxwellian distribution at the steepened front. The inset in the top right-hand panel shows the electron VDF integrated in x over an interval $\Delta x = 3\, d_i$, at different positions in the simulation domain: centred at the location of discontinuity $x = 85\, d_i$ (blue line) and outside the discontinuity, at $x = 60\, d_i$ and $x = 95\, d_i$ (orange and green lines), where the VDF is Maxwellian. The electrons at the discontinuity show a flat-top distribution with enhanced number of electrons in that region as to maintain the quasi-neutrality of the system (we do not find evidence of charge–space separation in

https://doi.org/10.1017/S0022377823000120 Published online by Cambridge University Press

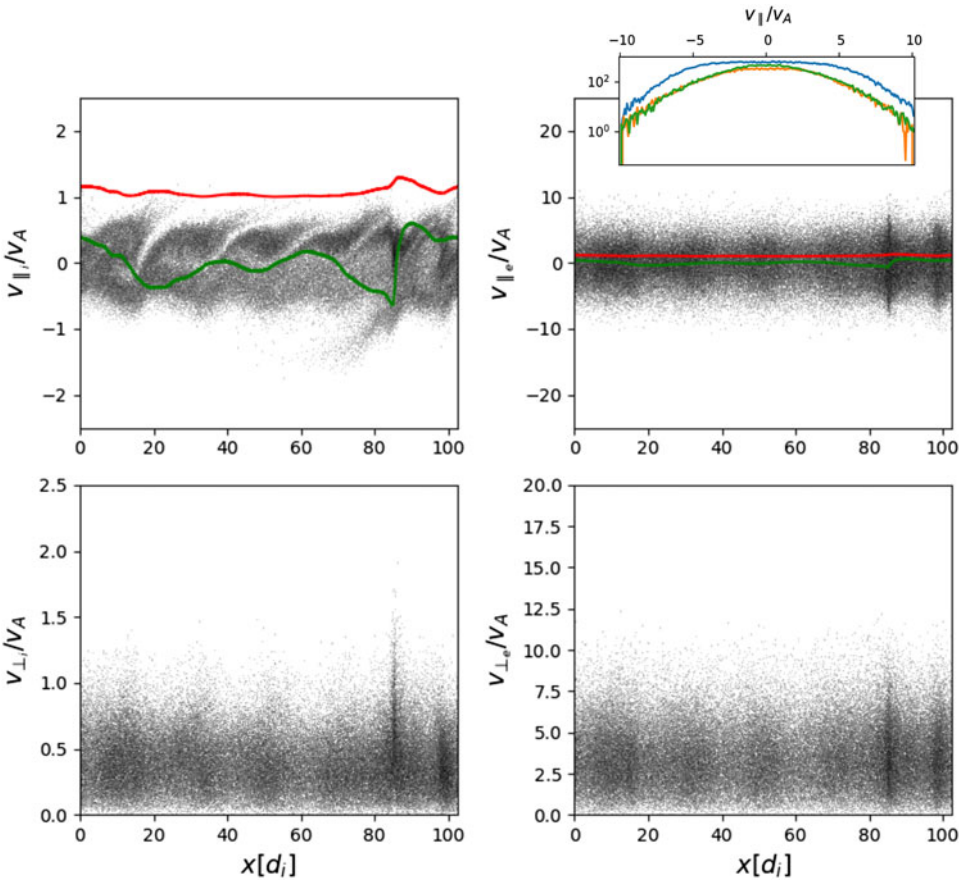

FIGURE 6. The phase space $(x, v_\parallel/v_\perp)$ for protons (left) and electrons (right). The phase space is shown at $t\Omega_{ci} = 400$ for Ecsim-TiTe4. The magnetic field's magnitude (red line) and B_y (green line) are also presented. The inset at top right represents the electron distribution function integrated in space around the discontinuity (blue) and outside the discontinuity (orange and green).

the simulations). We do not observe any electron beam in the simulations, and the electrons undergo on average isotropic heating.

4. Conclusions

We have investigated the PDI of a large-amplitude Alfvén wave with large-scale PIC simulations with an explicit (VPIC) and semi-implicit (ECsim) PIC code. Results from the PIC model are compared with those from a state-of-the-art hybrid model (CAMELIA) that employs an isothermal electron closure. Our main findings can be summarized as follows:

(*a*) The growth rate of the decay is determined by the total plasma beta in agreement with fluid theory. The electron temperature affects compressibility in a way that is consistent with the generalized Ohm's law. The higher the value of T_e, the larger the r.m.s. of the field-aligned electric field, and the lower the r.m.s. of density fluctuations.

https://doi.org/10.1017/S0022377823000120 Published online by Cambridge University Press

(*b*) Compressible effects lead not only to the generation of the ion-acoustic mode, but also to the development of a fast-mode steepened front propagating with the backward Alfvén wave. Particle interaction with those two types of compressible fluctuations leads to the increase of particle internal energy.

(*c*) Proton internal energy gain has contributions from: (i) phase-space mixing due to particle trapping by the ion-acoustic wave; (ii) beam acceleration aligned to the mean magnetic field at the steepened front; and (iii) particle scattering at the steepened front. Protons are overall heated preferentially in the parallel direction due to the contributions of particle trapping and beam formation. Electrons are also energized at the steepened front. Contrary to protons, electrons are heated isotropically.

(*d*) Analysis of the energy balance shows that after the complete decay of the pump wave 40 % of the pump wave goes into reflected wave, $\sim$ 50 % into proton internal energy (perpendicular and parallel) and $\sim$ 10 % into electron internal energy.

In conclusion, we have clarified that parametric decay can heat the plasma via two processes that in prior work (Araneda *et al.* 2008; Matteini *et al.* 2010*b*; González *et al.* 2020) were not as clearly separated as in this set of simulations. The processes are proton trapping and beam acceleration at steepened fronts. While proton trapping causes the energization of a proton population which propagates at the ion-sound speed, it is the steepened front that generates an actual beam at the Alfvén speed. Since the steepened front propagates backward due to the complete reflection of the pump wave, the beam also propagates backward in this set of simulations. Our results also provide the first energy balance analysis of parametric decay with fully kinetic simulations. In particular, we find that parametric decay preferentially heats protons, although electrons also gain a fraction of the energy stored in the pump wave. Heating triggered by parametric decay is consistent with the observed preferential proton heating with respect to electrons in the corona. In this context, our results provide a promising starting point to assess the role of (kinetic) compressible effects in wave-driven theories of the solar wind.

Acknowledgements

The authors acknowledge insightful discussions within the International Team ‘Heliospheric Energy Budget: From Kinetic Scales to Global Solar Wind Dynamics’ at the International Space Science Institute (ISSI) in Bern led by M.E.I. and A.T. We thank G. Lapenta and the ECSim development team for granting us access to the code. We also acknowledge the Texas Advanced Computing Center (TACC) at The University of Texas at Austin (http://www.tacc.utexas.edu) from providing computing time on Frontera and the Gauss Centre for Supercomputing e.V. (www.gauss-centre.eu) for providing computing time on the GCS Supercomputer SUPERMUC-NG at Leibniz Supercomputing Centre (http://www.lrz.de).

Editor F. Califano thanks the referees for their advice in evaluating this article.

Funding

This research was supported by NASA grant no. 80NSSC18K1211 and NSF award 2141564. M.E.I. acknowledges support from the German Science Foundation (DFG) within the Collaborative Research Center SFB1491.

Declaration of interests

The authors report no conflict of interest.

https://doi.org/10.1017/S0022377823000120 Published online by Cambridge University Press

REFERENCES

ARANEDA, J.A., MARSCH, E., ADOLFO, F. 2008 Proton core heating and beam formation via parametrically unstable Alfvén-cyclotron waves. *Phys. Rev. Lett*. **100** (12), 125003.

AUNAI, N., HESSE, M. & KUZNETSOVA, M. 2013 Electron nongyrotropy in the context of collisionless magnetic reconnection. *Phys. Plasmas* **20** (9), 092903.

BAUMJOHANN, W. & TREUMANN, R.A. 2012 *Basic Space Plasma Physics (Revised Edition)*. World Scientific Publishing Company.

BELCHER, J.W. & DAVIS, L. JR. 1971 Large-amplitude Alfvén waves in the interplanetary medium, 2. *J. Geophys. Res*. **76** (16), 3534–3563.

BOWERS, K.J., ALBRIGHT, B.J., BERGEN, B., YIN, L., BARKER, K.J. & KERBYSON, D.J. 2008*b* 0.374 pflop/s trillion-particle kinetic modeling of laser plasma interaction on roadrunner. In *SC'08: Proceedings of the 2008 ACM/IEEE conference on Supercomputing*, pp. 1–11. IEEE.

BOWERS, K.J., ALBRIGHT, B.J., YIN, L., BERGEN, B. & KWAN, T.J.T. 2008*a* Ultrahigh performance three-dimensional electromagnetic relativistic kinetic plasma simulation. *Phys. Plasmas* **15** (5), 055703.

BOWERS, K.J., ALBRIGHT, B.J., YIN, L., DAUGHTON, W., ROYTERSHTEYN, V., BERGEN, B. & KWAN, T.J.T. 2009 Advances in petascale kinetic plasma simulation with vpic and roadrunner. In *Journal of Physics: Conference Series*, vol. 180, p. 012055.

CAZZOLA, E., INNOCENTI, M.E., GOLDMAN, M.V., NEWMAN, D.L., MARKIDIS, S. & LAPENTA, G. 2016 On the electron agyrotropy during rapid asymmetric magnetic island coalescence in presence of a guide field. *Geophys. Res. Lett*. **43** (15), 7840–7849.

CHANDRAN, B.D.G. 2018 Parametric instability, inverse cascade and the $1/f$ range of solar-wind turbulence. *J. Plasma Phys*. **84** (1), 905840106.

COLEMAN, P.J. JR. 1967 Wave-like phenomena in the interplanetary plasma: mariner 2. *Planet. Space Sci*. **15** (6), 953–973.

CRANMER, S.R. 2012 Self-consistent models of the solar wind. *Space Sci. Rev*. **172** (1), 145–156.

CRANMER, S.R. 2020 Updated measurements of proton, electron, and oxygen temperatures in the fast solar wind. *Res. Not. AAS* **4** (12), 249.

DEL ZANNA, L. 2001 Parametric decay of oblique arc-polarized Alfvén waves. *Geophys. Res. Lett*. **28** (13), 2585–2588.

DEL ZANNA, L., MATTEINI, L., LANDI, S., VERDINI, A. & VELLI, M. 2015 Parametric decay of parallel and oblique Alfvén waves in the expanding solar wind. *J. Plasma Phys*. **81** (1).

DEL ZANNA, L. & VELLI, M. 2002 Coronal heating through Alfvén waves. *Adv. Space Res*. **30** (3), 471–480.

DEL ZANNA, L., VELLI, M. & LONDRILLO, P. 2001 Parametric decay of circularly polarized Alfvén waves: multidimensional simulations in periodic and open domains. *Astron. Astrophys*. **367** (2), 705–718.

DERBY, N.F. JR. 1978 Modulational instability of finite-amplitude, circularly polarized Alfven waves. *Astrophys. J*. **224**, 1013–1016.

ELLIOTT, H.A., HENNEY, C.J., MCCOMAS, D.J., SMITH, C.W. & VASQUEZ, B.J. 2012 Temporal and radial variation of the solar wind temperature' relationship. *J. Geophys. Res*. **117** (A9).

FRANCI, L., HELLINGER, P., GUARRASI, M., CHEN, C.H.K., PAPINI, E., VERDINI, A., MATTEINI, L. & LANDI, S. 2018 Three-dimensional simulations of solar wind turbulence with the hybrid code CAMELIA. *J. Phys.: Conf. Ser*. **1031**, 012002.

GALEEV, A.A. & ORAEVSKII, V.N. 1973 The stability of Alfven waves. *Sov. Phys. Dokl. Engl. Transl*. **7**, 988.

GEISS, J., GLOECKLER, G., VON STEIGER, R., BALSIGER, H., FISK, L.A., GALVIN, A.B., IPAVICH, F.M., LIVI, S., MCKENZIE, J.F., OGILVIE, K.W., *et al.* 1995 The southern high-speed stream: results from the swics instrument on ulysses. *Science* **268** (5213), 1033–1036.

GONZALEZ-HERRERO, D., BOELLA, E. & LAPENTA, G. 2018 Performance analysis and implementation details of the energy conserving semi-implicit method code (ecsim). *Comput. Phys. Commun*. **229**, 162–169.

https://doi.org/10.1017/S0022377823000120 Published online by Cambridge University Press

González, C.A., Tenerani, A., Matteini, L., Hellinger, P. & Velli, M. 2021 Proton energization by phase steepening of parallel-propagating Alfvénic fluctuations. *Astrophys. J. Lett*. **914** (2), L36.

González, C.A., Tenerani, A., Velli, M. & Hellinger, P. 2020 The role of parametric instabilities in turbulence generation and proton heating: hybrid simulations of parallel-propagating Alfvén waves. *Astrophys. J*. **904** (1), 81.

Hahn, M., Fu, X. & Savin, D.W. 2022 Evidence for parametric decay instability in the lower solar atmosphere. *Astrophys. J*. **933** (1), 52.

Hollweg, J.V. 1994 Beat, modulational, and decay instabilities of a circularly polarized Alfven wave. *J. Geophys. Res*. **99** (A12), 23431–23447.

Jayanti, V. & Hollweg, J.V. 1993 On the dispersion relations for parametric instabilities of parallel-propagating Alfvén waves. *J. Geophys. Res*. **98** (A8), 13247–13252.

Lapenta, G. 2017 Exactly energy conserving semi-implicit particle in cell formulation. *J. Comput. Phys*. **334**, 349–366.

Lapenta, G., El Alaoui, M., Berchem, J. & Walker, R. 2020 Multiscale mhd-kinetic pic study of energy fluxes caused by reconnection. *J. Geophys. Res*. **125** (3).

Lapenta, G., Gonzalez-Herrero, D. & Boella, E. 2017 Multiple-scale kinetic simulations with the energy conserving semi-implicit particle in cell method. *J. Plasma Phys*. **83** (2), 705830205.

Malara, F., Primavera, L. & Veltri, P. 2022 Parametric instability: an evolutive mechanism for the Alfvénic turbulence in the solar wind. *Universe* **8** (8), 391.

Matteini, L., Landi, S., Del Zanna, L., Velli, M. & Hellinger, P. 2010*a* Parametric decay of linearly polarized shear Alfvén waves in oblique propagation: one and two-dimensional hybrid simulations. *Geophys. Res. Lett*. **37** (20), L20101.

Matteini, L., Landi, S., Velli, M. & Hellinger, P. 2010*b* Kinetics of parametric instabilities of Alfvén waves: evolution of ion distribution functions. *J. Geophys. Res*. **115** (A9).

Matthews, A.P. 1994 Current advance method and cyclic leapfrog for 2d multispecies hybrid plasma simulations. *J. Comput. Phys*. **112** (1), 102–116.

Nariyuki, Y. & Hada, T. 2007 Consequences of finite ion temperature effects on parametric instabilities of circularly polarized Alfvén waves. *J. Geophys. Res*. **112** (A10).

Nariyuki, Y., Matsukiyo, S. & Hada, T. 2008 Parametric instabilities of large-amplitude parallel propagating Alfvén waves: 2d pic simulation. *New J. Phys*. **10** (8), 083004.

Perez, J.C. & Chandran, B.D.G. 2013 Direct numerical simulations of reflection-driven, reduced magnetohydrodynamic turbulence from the sun to the Alfvén critical point. *Astrophys. J*. **776** (2), 124.

Pezzi, O., Liang, H., Juno, J.L., Cassak, P.A., Vásconez, C.L., Sorriso-Valvo, L., Perrone, D., Servidio, S., Roytershteyn, V., TenBarge, J.M., *et al.* 2021 Dissipation measures in weakly collisional plasmas. *Mon. Not. R. Astron. Soc*. **505** (4), 4857–4873.

Réville, V., Tenerani, A. & Velli, M. 2018 Parametric decay and the origin of the low-frequency Alfvénic spectrum of the solar wind. *Astrophys. J*. **866** (1), 38.

Sakai, J.-I. & Sonnerup, B.U.O. 1983 Modulational instability of finite amplitude dispersive Alfvén waves. *J. Geophys. Res*. **88** (A11), 9069–9079.

Sakai, J.I., Yamamura, W., Saito, S., Washimi, H., Tsiklauri, D. & Vekstein, G. 2005 Particle simulation of plasma heating by a large-amplitude shear Alfven wave through its transverse modulation in collisionless plasmas. *New J. Phys*. **7** (1), 233.

Shoda, M., Suzuki, T.K., Asgari-Targhi, M. & Yokoyama, T. 2019 Three-dimensional simulation of the fast solar wind driven by compressible magnetohydrodynamic turbulence. *Astrophys. J. Lett*. **880** (1), L2.

Suzuki, T.K. & Inutsuka, S.-I. 2005 Making the corona and the fast solar wind: a self-consistent simulation for the low-frequency Alfvén waves from the photosphere to 0.3 au. *Astrophys. J*. **632** (1), L49.

Tenerani, A. & Velli, M. 2013 Parametric decay of radial Alfvén waves in the expanding accelerating solar wind. *J. Geophys. Res*. **118** (12), 7507–7516.

https://doi.org/10.1017/S0022377823000120 Published online by Cambridge University Press

VASQUEZ, B.J. & HOLLWEG, J.V. 1996 Formation of arc-shaped Alfvén waves and rotational discontinuities from oblique linearly polarized wave trains. *J. Geophys. Res*. **101** (A6), 13527–13540.

VERDINI, A., GRAPPIN, R. & MONTAGUD-CAMPS, V. 2019 Turbulent heating in the accelerating region using a multishell model. *Sol. Phys*. **294** (5), 1–18.

WILSON III, L.B., STEVENS, M.L., KASPER, J.C., KLEIN, K.G., MARUCA, B.A., BALE, S.D., BOWEN, T.A., PULUPA, M.P. & SALEM, C.S. 2018 The statistical properties of solar wind temperature parameters near 1 au. *Astrophys. J. Suppl. Ser*. **236** (2), 41.

WONG, H.K. & GOLDSTEIN, M.L. 1986 Parametric instabilities of circularly polarized Alfvén waves including dispersion. *J. Geophys. Res*. **91** (A5), 5617–5628.

https://doi.org/10.1017/S0022377823000120 Published online by Cambridge University Press